required for step (1) of the above mechanism, and assuming an additional 0.5 kcal mol^{-1} (ref. 18) to reduce the length of each of the three H-bonds in the OH$^-$(H$_2$O)$_3$ complex by 0.1 Å after step (1), an estimate of approximately 3 kcal mol^{-1} is obtained for the total activation energy of our mechanism. This rough estimate is consistent with the experimental value obtained from hydroxide mobility data[18].

The unexpectedly high coordination of the solvated hydroxide[2,23,26] contrasts with the textbook picture that each of the three lone pairs of O* accepts a single H-bond. An explanation of this phenomenon is obtained by analysing the electron localization function[29] along the mechanistic path of Fig. 3. The electron localization function indicates spatial regions where electron pairs are most likely to be found. The most striking feature of these functions (Fig. 3) is the presence of a continuous ring around the OH$^-$ bond axis[30,31]. This finding is corroborated by its electrostatic potential that displays a ring of maximum negative charge around its O terminus. This pattern, which suggests a lack of directionality in H-bonding to O*, supports both structural flexibility and high coordination, and is consistent with the spectroscopic picture of ref. 24.

The analysis presented here emphasizes the complex chemical differences between the hydrated H$_3$O$^+$ and OH$^-$ ions, and their effect on the anomalous transport mechanisms in acidic and basic solution (Fig. 1). We recognize the temptation to invoke symmetry arguments as a method to intuit mechanisms of seemingly similar processes. However, this approach cannot yield a correct picture when the chemistry of the two species is sufficiently different. Nevertheless, a common pattern of charge migration in acids and bases emerges: both require that the nascent species in the proton transfer process be correctly 'pre-solvated' by way of specific fluctuations in the local H-bond network.   □

1. Atkins, P. W. *Physical Chemistry* 6th edn 740–741 (Oxford Univ. Press, Oxford, 1998).
2. Tuckerman, M. E., Laasonen, K., Sprik, M. & Parrinello, M. *Ab initio* molecular dynamics simulation of the solvation and transport of H$_3$O$^+$ and OH$^-$ ions in water. *J. Phys. Chem.* **99,** 5749–5752 (1995).
3. Tuckerman, M. E., Laasonen, K., Sprik, M. & Parrinello, M. *Ab initio* molecular dynamics simulation of the solvation and transport of hydronium and hydroxide ions in water. *J. Chem. Phys.* **103,** 150–161 (1995).
4. Agmon, N. The Grotthuss mechanism. *Chem. Phys. Lett.* **244,** 456–462 (1995).
5. Marx, D., Tuckerman, M. E., Hutter, J. & Parrinello, M. The nature of the hydrated excess proton in water. *Nature* **397,** 601–604 (1999).
6. Marx, D., Tuckerman, M. E. & Parrinello, M. Solvated excess protons in water: quantum effects on the hydration structure. *J. Phys. Condens. Matter* **12,** A153–A159 (2000).
7. Vuilleumier, R. & Borgis, D. Transport and spectroscopy of the hydrated proton: A molecular dynamics study. *J. Chem. Phys.* **111,** 4251–4266 (1999).
8. Day, T. J. F., Schmitt, U. W. & Voth, G. A. The mechanism of hydrated proton transport in water. *J. Am. Chem. Soc.* **122,** 12027–12028 (2000).
9. Tuñón, I., Rinaldi, D., Ruiz-López, M. F. & Rivail, J. L. Hydroxide ion in liquid water: Structure, energetics, and proton transfer using a mixed discrete-continuum ab initio model. *J. Phys. Chem.* **99,** 3798–3805 (1995).
10. Muller, R. P. & Warshel, A. Ab initio calculations of free energy barriers for chemical reactions in solution. *J. Phys. Chem.* **99,** 17516–17524 (1995).
11. Hückel, E. Theorie der Beweglichkeiten des Wasserstoff- und Hydroxylions in wässriger Lösung. *Z. Elektrochem.* **34,** 546–562 (1928).
12. Eigen, M. Proton transfer, acid-base catalysis, and enzymatic hydrolysis. Part I: Elementary processes. *Angew. Chem. Int. Edn* **3,** 1–19 (1964).
13. Stillinger, F. H. in *Theoretical Chemistry: Advances and Perspectives* 177–234 (eds Eyring, H. & Henderson, D.) 177–234 (Academic, New York, 1978).
14. Zatsepina, G. N. State of the hydroxide ion in water and in aqueous solution. *J. Struct. Chem.* **12,** 894–898 (1971).
15. Schiöberg, D. & Zundel, G. Very polarizable hydrogen bonds in solution of bases having infra-red absorption continua. *J. Chem. Soc. Faraday Trans. II* **69,** 771–781 (1973).
16. Librovich, N. B., Sakun, V. P. & Sokolov, N. D. H$^+$ and OH$^-$ ions in aqueous solutions—Vibrational spectra of hydrates. *Chem. Phys.* **39,** 351–366 (1979).
17. Khoshtariya, D. E. & Berdzenishvili, N. O. A new dynamic elementary act model for thermal and photoinduced proton self-exchange through the lyate ion hydrogen bridges in solutions. *Chem. Phys. Lett.* **196,** 607–613 (1992).
18. Agmon, N. Mechanism of hydroxide mobility. *Chem. Phys. Lett.* **319,** 247–252 (2000).
19. Marx, D. & Parrinello, M. *Ab initio* path-integral molecular dynamics. *Z. Phys. B* **95,** 143–144 (1994).
20. Tuckerman, M. E., Marx, D., Klein, M. L. & Parrinello, M. Efficient and general algorithms for path integral Car-Parrinello molecular dynamics. *J. Chem. Phys.* **104,** 5579–5588 (1996).
21. Marx, D. & Hutter, J. in *Modern Methods and Algorithms of Quantum Chemistry* (ed. Grotendorst, J.) 301–449 (John von Neumann Institute for Computing, Forschungszentrum Jülich, 2000); also at ⟨http://www.theochem.ruhr-uni-bochum.de/go/cprev.html⟩ (2000).
22. Car, R. & Parrinello, M. Unified approach for molecular dynamics and density-functional theory. *Phys. Rev. Lett.* **55,** 2471–2474 (1985).
23. Novoa, J. J., Mota, F., del Valle, C. P. & Planas, M. Structure of the first solvation shell of the hydroxide anion. A model study using OH$^-$(H$_2$O)$_n$ (n = 4, 5, 6, 11, 17) clusters. *J. Phys. Chem. A* **101,** 7842–7853 (1997).
24. Chaudhuri, C. *et al.* Infrared spectra and isomeric structures of hydroxide ion-water clusters OH$^-$(H$_2$O)$_{1-5}$: a comparison with H$_3$O$^+$(H$_2$O)$_{1-5}$. *Mol. Phys.* **99,** 1161–1173 (2001).
25. Bruni, F., Ricci, M. A. & Soper, A. K. Structural characterization of NaOH aqueous solution in the glass and liquid states. *J. Chem. Phys.* **114,** 8056–8063 (2001).
26. Buchner, R., Hefter, G., May, P. M. & Sipos, P. Dielectric relaxation of dilute aqueous NaOH, NaAl(OH)$_4$ and NaB(OH)$_4$. *J. Phys. Chem.* **103,** 11186–11190 (1999).
27. Truhlar, D. G. & Kupperman, A. Exact tunneling calculations. *J. Am. Chem. Soc.* **93,** 1840–1851 (1971).
28. Tuckerman, M. E., Marx, D., Klein, M. L. & Parrinello, M. On the quantum nature of the shared proton in hydrogen bonds. *Science* **275,** 817–820 (1997).
29. Becke, A. D. & Edgecombe, K. E. A simple measure of electron localization in atomic and molecular systems. *J. Chem. Phys.* **92,** 5397–5403 (1990).
30. Trout, B. L. & Parrinello, M. Analysis of the dissociation of H$_2$O in water using first-principles molecular dynamics. *J. Phys. Chem. B* **103,** 7340–7345 (1999).
31. Liu, Y. & Tuckerman, M. E. Protonic defects in hydrogen bonded liquids: Structure and dynamics in ammonia and comparison with water. *J. Phys. Chem. B* **105,** 6598–6610 (2001).
32. Geissler, P. L., Dellago, C., Chandler, D., Hutter, J. & Parrinello, M. Autoionization in liquid water. *Science* **291,** 2121–2124 (2001).

Competing interests statement

The authors declare that they have no competing financial interests.

Correspondence and requests for materials should be addressed to M.E.T. (e-mail: mark.tuckerman@nyu.edu).

Nonlinear dynamics of ice-wedge networks and resulting sensitivity to severe cooling events

L. J. Plug* & B. T. Werner

Complex Systems Laboratory, Cecil and Ida Green Institute of Geophysics and Planetary Physics, University of California San Diego, La Jolla, California 92093-0225, USA

Patterns of subsurface wedges of ice that form along cooling-induced tension fractures, expressed at the ground surface by ridges or troughs spaced 10–30 m apart, are ubiquitous in polar lowlands[1]. Fossilized ice wedges, which are widespread at lower latitudes, have been used to infer the duration[2–4] and mean temperature[5,6] of cold periods within Proterozoic[2] and Quaternary climates[3–13], and recent climate trends have been inferred from fracture frequency in active ice wedges[14]. Here we present simulations from a numerical model for the evolution of ice-wedge networks over a range of climate scenarios, based on the interactions between thermal tensile stress, fracture and ice wedges. We find that short-lived periods of severe cooling permanently alter the spacing between ice wedges as well as their fracture frequency. This affects the rate at which the widths of ice wedges increase as well as the network's response to subsequent climate change. We conclude that wedge spacing and width in ice-wedge networks mainly reflect infrequent episodes of rapidly falling ground temperatures rather than mean conditions.

Ice wedges originate with fractures opened in perennially frozen ground by tensile stress induced by falling winter temperatures[15–17].

* Present address: Department of Earth Sciences, Dalhousie University, Halifax B3H 4R2, Canada.

Fractures partially fill with ice from blowing or thawing snow, and then close when the ground warms[16,17]. Because ice in fracture cavities is generally weaker than frozen ground, fractures usually follow the same path from year to year[3,16–18]. Over thousands of years, V-shaped wedges of ice 3–5 m deep and up to several metres wide develop along recurring fracture paths[3]. Upward deformation at the ground surface forms ridges with heights ranging from decimetres to 1 m, revealing the position of growing ice wedges below[3].

Although these basic processes relating to a single ice wedge have been the focus of previous investigations[15–18], the development of network patterns over longer timescales and their relationship to varying climates remains uncertain. The nonlinearity of fracture initiation and propagation, the influence of open fractures on subsequent fracturing during a single winter, and the long-term memory of fracture patterns from past winters stored in ice wedges all constitute building blocks of a system that could exhibit complex dynamical behaviour diverging from that of a single ice wedge.

Reflecting the essentially two-dimensional nature of ice-wedge networks[19], we model fractures and ice wedges using a two-dimensional array of cells representing the top approximately five metres of frozen ground. Each cell contains either frozen ground or ice, and can contain a segment of an open fracture. All cells initially are assigned unfractured frozen ground, and thereafter evolve through repeated application of an algorithm that corresponds to one year in the model (Methods). To represent the thermal tensile stress that gives rise to fractures in frozen ground, a pre-fracture tensile stress (the thermal stress without reduction by fractures) that is uniform across the model lattice is incremented from 0 MPa to a specified maximum value. Fracture segments locally reduce this tensile stress by an amount that is proportional to the inverse square of distance and is maximized along a line perpendicular to the segment[15,19]. As thermal stress increases, fractures initiate in cells where local stress

exceeds strength, and propagate cell-by-cell in two opposing directions along directions determined by stress imposed by open fracture segments, parameterized heterogeneity, and the energetic cost of propagation (higher in frozen ground than in ice). At the end of a fracture episode, the width of ice wedges is increased in cells with open fractures, all open fractures are closed, and values of tensile strength and propagation threshold are set to those for ice in all cells that contain fractures. The effect of a growing ice wedge on the ground surface is modelled by deforming the surface over the wedge by a volume equal to the volume of ice added. The relaxation
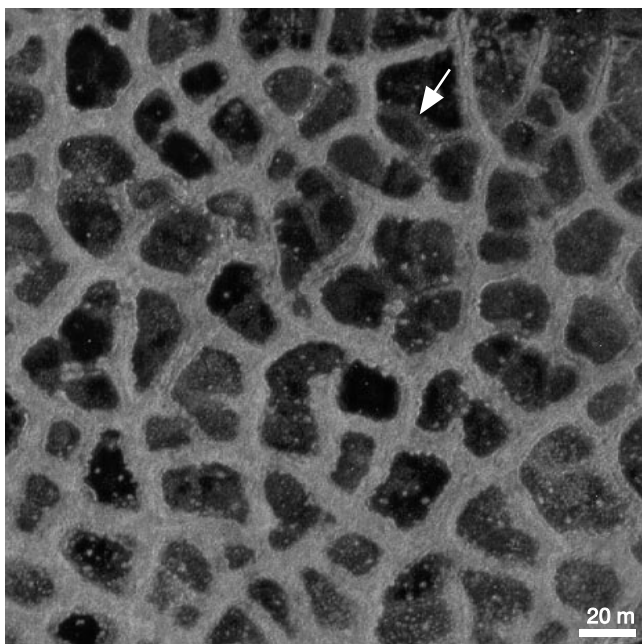

Figure 2 Fracture pattern after 1 yr, and surface elevation after 2,000 yr, for three model experiments. Left panels show fractures, right panels show height. The models are a uniform-stress network (**a**), a narrow-range network (**b**), and a lake-floor network (**c**). Arrow at bottom right indicates a low ridge developed over a modelled ice wedge that infrequently fractures. Relief below 0.2 m is shown black, representing shallow standing water common in many natural networks (see, for example, Fig. 1). All simulations use domains of 250 × 250 1-m² cells. To minimize variations between networks owing to random variations in first fractures rather than stress history, all simulations use the same random seed; hence, paths of long initial fractures are similar. Distributions of wedge spacing and orientation from the uniform-stress model at 2,000 yr (defined by a threshold ridge height of 0.3 m) match similarly sized regions of natural networks at Espenberg, Alaska, as evaluated with a two-dimensional Kolmogorov–Smirnov test[19]. Unlike most natural networks, modelled networks exhibit increased height (lighter patches) over some intersections between ice wedges. Possibly, natural ice-wedge growth increments near intersections are smaller because of nonlinear tensile stress reduction in the complicated region of an intersection, an effect not included in the model.

Figure 1 Near-infrared aerial photograph of an ice-wedge network on the floor of a drained lake near Espenberg, northwest Alaska. Ridges (0.25–1 m high, spaced 10–30 m apart) overlie ice wedges, and appear light because they are dry and covered by herbaceous vegetation. Troughs appear dark because of wet sedge-tundra vegetation or standing water. Arrow indicates low, barely visible ridge (see Fig. 2c and text). Photograph provided by the National Park Service.
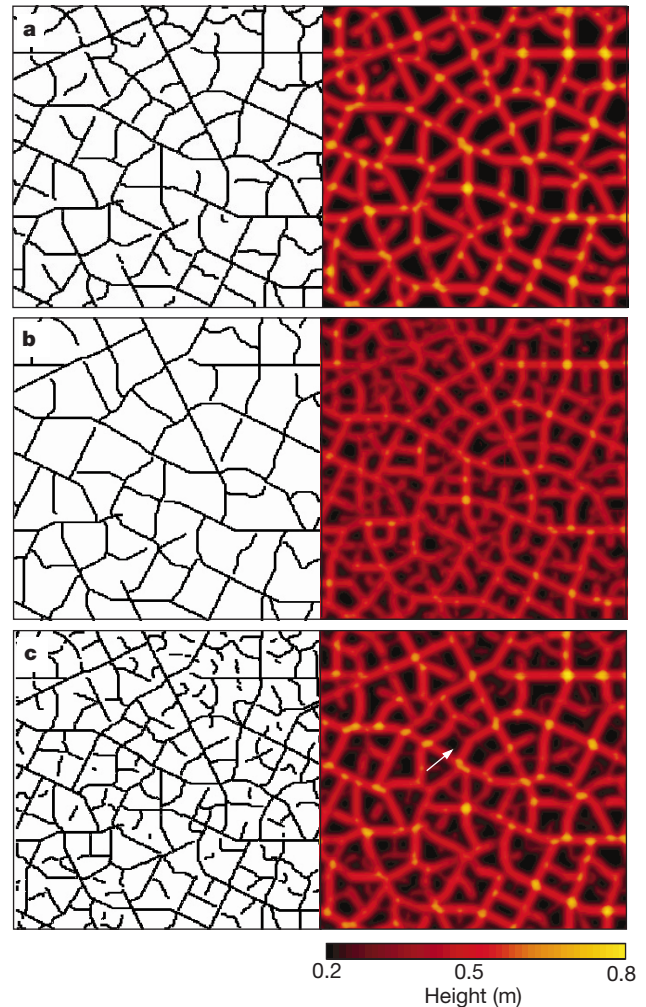
of morphology by soil creep is modelled with linear diffusion. The values of parameters were chosen to be consistent with existing measurements (Methods), many with broad uncertainties. Model results are not highly sensitive to parameter values[19].

Our goal is to model the development of ice-wedge networks over thousands of years. Details pertaining to the shorter-timescale dynamics of fracture propagation, tensile stress field and frozen ground deformation are simplified or omitted, on the basis of the hypothesis that dynamics of these processes dissipate on the longer timescales of the pattern of interest[20,21], the ice-wedge network. This assumption is supported by comparisons of modelled to natural ice-wedge networks (Figs 1 and 2). In both modelled and natural networks, ice wedges range from long and sinuous to short and straight. Many ice wedges terminate at orthogonal intersections with other wedges, but some paths cross, forming four-way junctions. The spacing (15–20 m) and relative orientation (Fig. 3) of surface ridges and the mean width of ice wedges after 2,000 yr (1–3 m) are consistent with measured values from ice-wedge networks in northern Alaska and Canada[3,19]. The similarity between natural networks and networks modelled using reasonable parameter values (Methods), and the relative insensitivity of model results to parameter values[19], suggest that dynamics of modelled networks can be used to investigate natural networks, despite some parameters being poorly constrained by measurements (Methods). Qualitative model-based inferences are most robust.

The response of modelled networks to changes and variability in climate was investigated using four numerical experiments in which only the sequence of maximum annual stress was varied. In the first experiment, the severity of each winter's cooling episode was fixed by setting maximum tensile stress to the same value, 2 MPa, each year. The resultant ice-wedge network diverges from the initial fracture pattern (Fig. 2a), as illustrated by a decrease in spacing between ice wedges from 21.7 m in the first year to 19.2 m after 800 yr (Fig. 3a). Although most fractures are constrained to ice wedges, the divergence in spacing arises as different permutations in the order of ice-wedge fracturing permit the introduction of new fracture paths and hence new wedges. These new fractures open at locations where tensile stress exceeds the strength of frozen ground before fractures that reduce the regional tensile stress open in nearby ice wedges. Switching the sequence of fracturing in two ice wedges can convert an orthogonal three-way (T-type) intersection into a crossing four-way intersection; in this case, the wedge that terminates at the T can be extended if it fractures before the perpendicular wedge. After approximately 800 yr, the modelled ice-wedge network attains a steady state, characterized by consistent spacing between fractures, ice wedges and surface ridges. 88% of ice wedges fracture each year, a frequency sufficient to form ridges more than 0.3 m high at the surface over all ice wedges. Long ice wedges tend to fracture more frequently because they contain more potential sites for fracture initiation, and because a fracture, once initiated in a wedge, generally propagates along its entire length. Open fractures in these long wedges reduce tensile stress in nearby short wedges, lowering their fracture frequency. The width of ice wedges reaches 2.8 ± 0.7 m after 2,000 yr, the high standard deviation reflecting the variation in frequency with which ice wedges fracture and the addition of new wedges during the first 800 yr. The width and frequency of fracture of ice wedges decrease as the ratio of ice strength to ground strength increases in the model; we expect that the values provided here are upper limits.

To investigate the sensitivity of ice-wedge width and spacing to climate variability, two experiments with maximum annual stress normally distributed around a mean of 2 MPa were performed, with standard deviation (s.d.) = 1 MPa (narrow-range) and s.d. = 1.75 MPa (broad-range). The pattern of ice wedges in the narrow-range network reaches an approximate steady state after about 1,200 yr, with a spacing between ice wedges of 13.1 m (Fig. 3b), whereas the broad-range network only attains approximate steady state after 1,800 yr, with ice wedges separated by 12.0 m (Fig. 3c). The fraction of ice wedges that fracture in a given year is reduced from, and more variable than, the fraction for the uniform-stress network: $57 \pm 15\%$ for the narrow-range network, and $48 \pm 23\%$ for the broad-range network. Spacing between surface ridges after 2,000 yr is 15.7 m for the narrow-range network and 16.8 for the broad-range network (Fig. 3b, c). These spacing values are intermediate between mean annual fracture spacing and ice-wedge spacing, because not all wedges added during high-stress winters fracture with sufficient frequency during subsequent winters to form ridges. Counter to intuition, ridge spacing in the broad-range network is greater than ridge spacing in the narrow-range network, despite reduced ice-wedge spacing. This reflects greater over-saturation by ice wedges in the broad-range network; therefore, fewer ice wedges fracture with sufficient frequency to form ridges. The patterns of surface ridges of both broad- and narrow-range networks achieve steady state more than 600 yr after the corresponding ice-wedge patterns; this is because ice wedges added during high-stress years are expressed at the surface only after many episodes of refracture.

The sensitivity of ice-wedge networks to conditions at their time of initiation is illustrated in an experiment in which maximum tensile stress was set to 4 MPa for the first 4 yr of network development and to 0.8 MPa (below the fracture initiation threshold in frozen ground) thereafter. This scenario corresponds to network development following draining of a thaw lake[22], in which minimal insulating snow accumulates in the wind-swept basin during the first winters after desiccation, but accumulation increases to approximately 0.5 m after 5 yr as snow-trapping plants colonize the basin[16]. Spacing of modelled wedges reaches 16.3 m after 4 yr (Figs 2c, 3d), and remains constant thereafter because the maximum tensile stress is below frozen ground strength. Despite developing principally under a maximum stress insufficient to fracture frozen ground, ice wedges in the lake-floor network grow at a rate comparable to that in other numerical experiments. More so than in the other experiments, ice wedges that are long, and therefore contain more potential sites for fracture initiation, tend to fracture
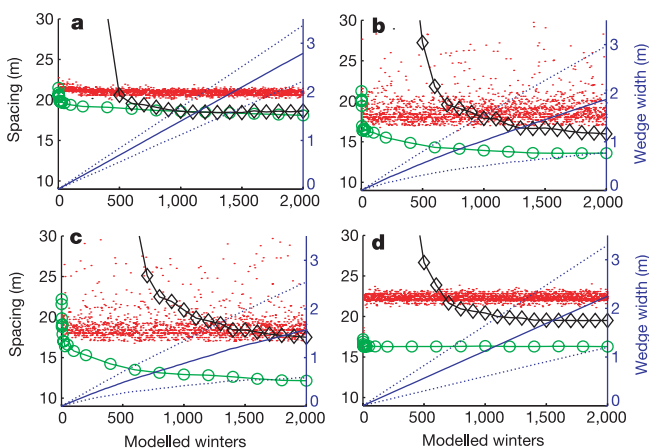

Figure 3 Properties of ice-wedge and fracture patterns versus time for four modelled networks. **a**, Uniform-stress network; **b**, narrow-range network; **c**, broad-range network; and **d**, lake-floor network. Green circles, spacing between ice wedges; red dots, spacing between fractures in the annual fracture pattern; black diamonds, spacing between surface ridges that form over wedges; blue lines, width of ice wedges (solid line, mean; dotted line, 1 s.d. envelope). Spacing is the median of 1,000 measurements of distance between fractures or ice wedges, measured along sample lines that cross a network at randomly selected angles and originate from randomly selected locations[19]. Spacing of surface ridges is measured between centre-lines of ridges at the 0.30-m contour interval, a height that approximates the characteristic roughness of tussock tundra surfaces.

with greater frequency than short wedges. Short ice wedges that rarely fracture do not appear (or barely appear) in the visual pattern of surface ridges because of relaxation of ground surface morphology (Fig. 2c). The spacing between surface ridges, 19.4 m, is consequently 20% greater than ice-wedge spacing (Fig. 3d).

We interpret these results as having the following implications. First, metre-wide fossil wedges indicate the existence (for at least thousands of years) of permafrost and conditions sufficient to fracture wedge ice; but they do not necessarily indicate sustained conditions sufficiently harsh to fracture frozen ground, because a brief exposure to high-tensile-stress conditions can lead to the formation of an ice-wedge network that then continues to develop under conditions insufficient for initial formation. Because networks are sensitive to initial and extreme conditions, the geographical distribution of networks might not correlate with mean climate, as has been suggested for modern[10] and fossil[2–10] networks. Second, wedge spacing[7] mainly reflects infrequent severe winter conditions (periods of rapidly falling air temperature at low absolute temperature) during the formation of the network, because episodes of high maximum tensile stress add new wedges to a network. Third, measurements of ice-wedge width[2–4] might provide minimum limits to the duration of cold climates, but the maximum duration is uncertain because growth rates are reduced by climatic variability and are widely variable between ice wedges. Long wedges are the most reliable measure of network duration because they form early in network development. Narrow fossil wedges are consistent with a cold, inherently variable climate, or with a moderate climate marginally suitable for ice-wedge development[5,6]. Fourth, low rates of fracture in networks[4,18] are consistent with a stationary but inherently variable climate, as well as with other climate scenarios, and so alone cannot be used to infer climate change. However, changes in fracture frequency across a population of ice wedges[14], sustained over many winters, are consistent with climate change.

The characteristics of ice-wedge networks reflect an interplay between fracturing, ice-wedge growth and network development, all nonlinear processes with differing intrinsic timescales. Our model for the evolution of ice-wedge networks shows complex behaviour under a range of climate scenarios. This suggests the need for caution in inferring the response of ice-wedge networks (and that of other, more complicated, geomorphic systems) to climate change using simple models or conceptions of their behaviour. □

Methods

Stress

Thermal tensile stress in frozen ground is a complicated function of material-dependent rheology, absolute temperature and rate of cooling, and is highly uncertain in field settings. The maximum annual stress used for the uniform stress model, 2 MPa, is based on a viscoelastic rheological model for frozen ground before fracture[15], a cooling rate of $10\,°C\,d^{-1}$ and a quasi-viscous parameter, $\bar{n}$, of $8 \times 10^{25}\,N^3\,m^{-6}\,s$, where $\bar{n}$ relates the rate of permanent quasi-viscous strain $\dot{E}$ under a constant sustained stress P in $P^3 = 2\bar{n}\dot{E}$ (ref. 15). An increase of maximum annual stress to 3.75 MPa, used as the $+1$ s.d. limit in the broad-range network, might be caused by a decrease in the absolute ground temperature from $-10\,°C$ to $-30\,°C$, with a corresponding increase in $\bar{n}$ to $15 \times 10^{25}\,N^3\,m^{-6}\,s$ (ref. 15). Changes in absolute ground temperature are one route to changes in maximum annual tensile stress, and changes in the rate of temperature change are another[15].

Local tensile stress, $\sigma_{kl}(\theta)$, the stress perpendicular to angle θ in cell kl, is taken to be pre-fracture thermal tensile stress, σ_T, minus the sum of reductions from nearby open fracture segments in cells ij, according to

$$\sigma_{kl}(\theta) = \sigma_T \left(1 - \sum_{ij} \frac{C}{(d_{ijkl})^n} \cos(\beta_{ijkl}) \sin(\alpha_{ijkl})\right) \qquad (1)$$

where d_{ijkl} is the distance (in m) from the centre of cell ij to the centre of cell kl, β_{ijkl} is the difference between the angle of the fracture in cell ij and angle θ, and α_{ijkl} is the angle between the line segment connecting cell kl and cell ij and the normal to the fracture segment in cell ij (ref. 19). Parameters are set to $n = 2$ and $C = 3\,m^2$ so that far-field modelled stress approximates the solution to two-dimensional elastic equations for stress around an infinitely long, straight fracture 4 m deep[15,19].

Fracture

Fractures are initiated where local tensile stress exceeds strength (set to 1 MPa for frozen

ground and 0.3 MPa for ice wedges, values chosen from the small range of laboratory measurements of small samples of ice and frozen silt[19,23,24], because *in situ* measurements of wedge ice and heterogeneous soil are lacking). Once initiated, fractures continue to propagate if the elastic strain energy released by opening of the fracture, G, exceeds the energy required to create new fracture surfaces, G_o, set to $1.5\,J\,m^{-2}$ in ice-wedge cells[25] and to $8\,J\,m^{-2}$ in frozen ground cells[19]. Both values have large uncertainties; their ratio determines the degree to which fractures tend to follow wedges. G is calculated from the pre-fracture tensile stress along the 5 m of fracture path preceding the position of the fracture tip, linearly weighted toward stresses near the tip, and from modelled shear stress across the fracture plane at the fracture tip[19]. The angle of fracture propagation is re-evaluated as a fracture tip enters a new cell, with $P(\theta,\Delta\theta)$, the probability that propagation angle changes from θ to $\theta + \Delta\theta$, given by a Boltzmann factor $\exp[\Delta G(\theta + \Delta\theta)/G_{random}]$. Here $\Delta G(\theta + \Delta\theta)$ is the change in net energy ($G - G_o$) released as a function of change in propagation angle and G_{random} parameterizes the magnitude of heterogeneity in frozen ground and in tensile stress. G_{random} is set to $0.5\,J\,m^{-2}$ so that isolated fractures in the model follow irregular paths similar to paths of first fractures in frozen ground[16,19].

Ice-wedge and surface dynamics

The width of ice wedges is increased in cells with open fractures by a positive amount drawn from a normal distribution with both mean and standard deviation 0.0015 m (ref. 3). The effect of a growing ice wedge on the ground surface is modelled by raising the surface over the wedge by a volume equal to the volume of ice added, with the depth of fractures assumed to be 4 m. This elevation increment has a gaussian shape centred on the axis of the ice wedge, with standard deviation equal to the wedge width[3]. This approach assumes the common natural case of a ridge over an ice wedge. Other modes of deformation can result in different morphologic responses[1]; however, the cause of differences between them is poorly understood and is not the subject of our investigation. Measurements of morphologic relaxation in permafrost are lacking; we model relaxation as diffusion[26] with diffusion constant $5 \times 10^{-3}\,m^2\,yr^{-1}$.

1. French, H. M. *The Periglacial Environment* (Addison Wesley, Harlow, 1996).
2. Williams, G. E. *et al.* in *Earth's Glacial Record* (eds Deynoux, M. *et al.*) 146–164 (Cambridge Univ. Press, Cambridge, 1994).
3. Black, R. F. in *Glacial Geomorphology* (ed. Coates, D.) 247–275 (State Univ. New York, Binghamton, 1974).
4. Johnson, W. H. Ice-wedge casts and relic patterned ground in central Illinois and their environmental significance. *Quat. Res.* **33,** 51–72 (1990).
5. Renssen, H. & Isarin, R. F. B. The two major warming phases of the last deglaciation at ~14.7 and ~11.5 ka cal BP in Europe: climate reconstructions and AGCM experiments. *Glob. Planet. Change* **30,** 117–153 (2001).
6. Isarin, R. F. B. Permafrost distribution and temperatures in Europe during the Younger Dryas. *Permafrost Periglac. Process* **8,** 313–333 (1997).
7. Maizels, J. K. Frequency of relic frost-fissure structures and prediction of polygon pattern: A quantitative approach. *Biul. Peryglac.* **30,** 67–89 (1986).
8. Walters, J. C. Ice-wedge casts and relict polygonal patterned ground in North-East Iowa, USA. *Permafrost Periglac. Process* **5,** 269–282 (1994).
9. Owen, L. A. *et al.* Relic permafrost structures in the Gobi of Mongolia: age and significance. *J. Quat. Sci.* **13,** 539–547 (1998).
10. Pewe, T. L. *Proc 1st Int. Permafrost Conf.* 76–81 (Publication 1287, National Academy of Science and National Research Council, Washington DC, 1966).
11. Black, R. F. Periglacial features indicative of permafrost: Ice and soil wedges. *Quat. Res.* **6,** 3–26 (1976).
12. Borns, H. W. Late glacial ice-wedge casts in northern Nova Scotia, Canada. *Science* **148,** 1223–1226 (1965).
13. Grosso, S. A. & Corte, A. E. Pleistocene ice wedge casts at 34 degrees S; Eastern Andes piedmont, south-west of South America. *Geogr. Ann. A* **71,** 125–136 (1989).
14. Kasper, J. N. & Allard, M. Late-Holocene climatic changes as detected by the growth and decay of ice wedges on the southern shore of Hudson Strait, northern Québec, Canada. *Holocene* **11,** 563–577 (2001).
15. Lachenbruch, A. H. Mechanics of thermal contraction cracks and ice-wedge polygons in permafrost. *Spec. Pap. Geol. Soc. Am.* **70** (1962).
16. Mackay, J. R. The first seven years (1978-1985) of ice-wedge growth; Illisarvik experimental drained lake site, western Arctic coast. *Can. J. Earth Sci.* **23,** 1782–1795 (1986).
17. Mackay, J. R. Air temperature, snow cover, creep of frozen ground, and the time of ice-wedge cracking, western Arctic coast. *Can. J. Earth Sci.* **30,** 1720–1729 (1993).
18. Mackay, J. R. The frequency of ice-wedge cracking (1967–1987) at Garry Island, western Arctic coast, Canada. *Can. J. Earth Sci.* **29,** 236–248 (1992).
19. Plug, L. J. & Werner, B. T. Fracture networks in frozen ground. *J. Geophys. Res.* **106,** 8599–8613 (2001).
20. Werner, B. T. Complexity in natural landform patterns. *Science* **284,** 102–104 (1999).
21. Nicolis, G. & Prigogine, I. *Self-organization in Nonequilibrium Systems* (Wiley, New York, 1977).
22. Hopkins, D. M. Thaw lakes and thaw sinks in the Imuruk Lake area, Seward Peninsula Alaska. *J. Geol.* **57,** 119–131 (1949).
23. Zhu, Y. & Carbee, D. L. *Tensile Strength of Frozen Silt* Report 87-14 (Army Cold Regions Research and Engineering Laboratory, Hannover, New Hampshire, 1987).
24. Gold, L. W. Engineering properties of freshwater ice. *J. Glaciol.* **19,** 197–212 (1977).
25. Goodman, D. J. & Tabor, D. Fracture toughness of ice: An account of some new experiments. *J. Glaciol.* **21,** 651–660 (1978).
26. Hanks, T. C., Bucknam, R. C., Lajoie, K. R. & Wallace, R. E. Modification of wave-cut and faulting controlled landforms. *J. Geophys. Res.* **89,** 5771–5790 (1984).

Acknowledgements

....

Waning buoyancy in the crustal roots of old mountains

Karen M. Fischer

Department of Geological Sciences, Brown University, Providence, Rhode Island 02912, USA

....

When mountains form through the collision of lithospheric plates, uplift of the Earth's surface is accompanied by thickening of the crust, and the buoyancy of these deep crustal roots (relative to the surrounding mantle) is thought to contribute to the support of mountain topography. Once active tectonism ceases, continuing erosion will progressively wear away surface relief. Here I provide new constraints on how crustal roots respond to erosional unloading over very long timescales. In old collisional mountain belts, ratios of surface relief to the thickness of the underlying crustal root are observed to be smaller than in young mountains. On the basis of gravity data, this trend is best explained by a decrease in the buoyancy of the crustal root with greater age since the most recent mountain-building episode—which is consistent with metamorphic reactions[1,2] produced by long-term cooling. An approximate balance between mountain and root mass anomalies suggests that the continental lithosphere remains weak enough to permit exhumation of crustal roots in response to surface erosion for hundreds of millions of years. The amount of such uplift, however, appears to be significantly reduced by progressive loss of root buoyancy.

Processes such as lithospheric delamination and rifting may strip away the crustal roots of some collisional mountain regions, but substantial crustal roots have survived in many mountain belts over hundreds of millions to billions of years[3–13]. Unless the lithosphere is mechanically very rigid, post-tectonic erosion of mass from the surface should be accompanied by some uplift of a buoyant crustal root and inflow of mantle. If the lithosphere is very weak, the region should be in local isostatic equilibrium, and the net change in mass over time would be zero. To examine how mountain crustal roots evolve over time, surface relief, crustal thickness and gravity data were compared in young collisional mountain belts and in old orogens where some crustal root is preserved. Crustal thickness was constrained seismically, primarily by refraction and reflection studies but in a few cases by teleseismic receiver function and surface wave analyses[3–22].

Ratios of surface relief (h) to crustal root magnitude (m) reveal a pronounced secular trend (Figs 1 and 2). In active or very young collisional orogens such as the Alps, Carpathians, Tien Shan and the Tibetan Plateau[17–22], these ratios (R) span a wide range, but are systematically higher than in older orogenic belts, particularly those where contraction ceased more than 100 million years (Myr) ago (Fig. 1a). Substantial zones of thickened crust are observed beneath some Proterozoic age orogens[10–13]. Little to no topography is associated with these apparent crustal roots, and thus R values for these regions lie close to zero. The decrease in R with age becomes
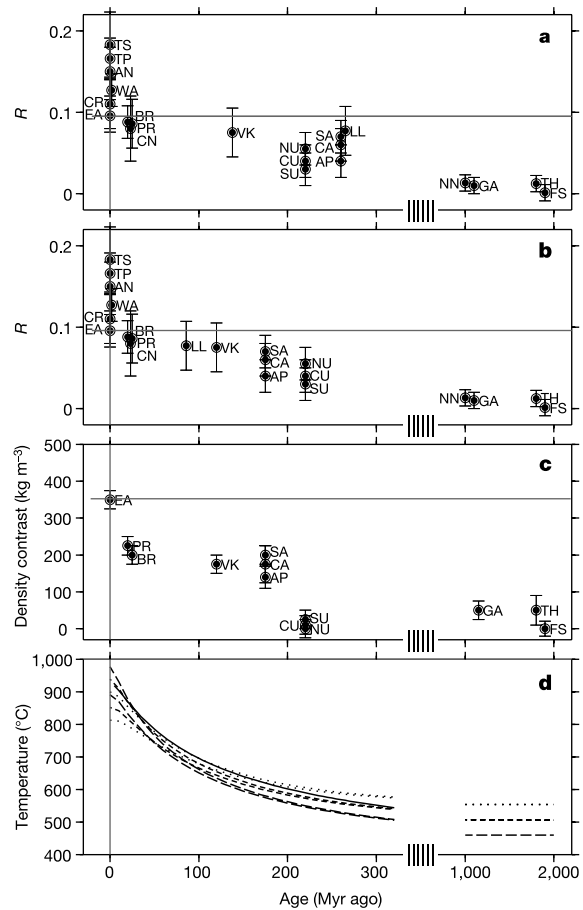

Figure 1 Comparison of surface topography to crustal root thickness, crustal root buoyancy, and crustal root temperature for young and old collisional mountain belts. **a**, Ratios (R) of mountain surface relief (h) to crustal root thickness (m) as a function of the time since collision ceased. **b**, R values as a function of time since the last major thermotectonic event in the region. **c**, Differences between crustal root and mantle density that best fit observed Bouguer gravity anomalies, assuming the seismically constrained shape of the crustal root and allowing a single value for upper crust density to vary. Error bars are 95% confidence limits. TP, Tibetan Plateau; TS, Tien Shan; AN, central Andes; WA, western Alps; CR, Carpathians; EA, eastern Alps; PR, central Pyrenees; BR, Brooks range; CN, Cantabrian mountains; VK, Verkhoyansk mountains; NU, northern Urals; CU, central Urals; SU, southern Urals; SA, southern Appalachians; CA, central Appalachians; AP, Appalachian Plateau; LL, Lachlan Orogen; NN, Namaqua–Natal Orogen; GA, northwest Grenville Orogen; TH, Trans-Hudson Orogen; FS, Svecofennian Orogen. **d**, Temperature at the Moho for a 45-km-thick crust from analytical and finite difference cooling models. Analytical calculations cool from a geotherm parameterized by initial surface heat flow (q_0) and crustal heat production (A) to an infinite time geotherm with lower heat flow (q_f) but the same A value; q_f of 50 mW m^{-2} and A of 0.8 μW m^{-3} (dotted lines); q_f of 45 mW m^{-2} and A of 0.7 μW m^{-3} (short dashed lines); q_f of 40 mW m^{-2} and A of 0.6 μW m^{-3} (long dashed lines). In each case q_0 values of 70 mW m^{-2} and 65 mW m^{-2} correspond to the hotter and cooler initial geotherm, respectively. Initial thermal lithospheric thicknesses are 60–90 km and final thicknesses are 190–230 km. In the one-dimensional finite difference calculation (solid line) a starting geotherm (q_0 of 70 mW m^{-2} and A of 0.7 μW m^{-3}) over a half-space was allowed to cool freely given continuous constant crustal heat production. For cooling since 320 Myr ago or later, finite difference cooling rates are comparable to the analytical calculation with the same q_0 and A, but slightly slower. Over longer times, the finite difference model continues to cool to unreasonably low heat flow and large lithospheric thickness, and is not shown. Conductivity in all cases is 2.6 W m^{-1}°C^{-1}, and mantle potential temperature is 1,300 °C with an adiabatic gradient of 0.3 °C km^{-1}. These calculations are not meant to replicate the temperature history of specific orogens. Rather, they are intended to show that significant cooling is possible over 200–300-Myr timescales.